PAPER • OPEN ACCESS

Influence of wakes interaction and upstream turbulence on three tidal turbines behaviour

To cite this article: M-A Dufour *et al* 2024 *J. Phys.: Conf. Ser.* **2767** 052017

Influence of wakes interaction and upstream turbulence on three tidal turbines behaviour

M-A Dufour[1,2], G Pinon[1], E Rivoalen[1,3] and G Germain[2]

[1] Laboratoire Ondes et Milieux Complexes (LOMC) - Normandie Univ, UNIHAVRE, CNRS, 76600 Le Havre, France
[2] Laboratoire d'Hydrodynamique Marine (LHyMar), IFREMER, Centre Manche Mer du Nord, 62200 Boulogne-sur-Mer, France
[3] Laboratoire de Mécanique de Normandie (LMN) - Normandie Univ, INSA ROUEN, LMN, 76000 Rouen, France

E-mail: `gregory.pinon@univ-lehavre.fr`

Abstract. The current study presents numerical results on three tidal turbine models (two in front, one downstream) interacting in a turbulent upstream flow. The numerical results come from a lifting-line (LL) embedded in a Lagrangian vortex particle (VP) solver: Dorothy LL-VP. The objective is to assess the extent to which this numerical tool is suited to reproduce accurately wakes interaction as well as fluctuating loads perceived by the downstream turbine. To this aim, the numerical set-up reproduces an experimental campaign led at IFREMER's wave and current flume tank. The downstream turbine is placed at different positions to change the wakes interaction. Two upstream turbulence intensities (TI) experimentally tested are reproduced numerically using the synthetic eddy method (SEM). Favourable comparisons are obtained between numerical and experimental wakes, including velocity profiles. Preliminary results suggest that the downstream turbine performance decrease is numerically well captured. More investigations are needed on the loads fluctuations with longer computation time, and adding an angular velocity controller as well as hub modelling to Dorothy LL-VP.

1. Introduction

Nowadays wind and tidal energy fields face similar challenges from a fluid dynamic point of view: upstream flow turbulence and turbine wakes interaction in array or farm conditions. This last challenge arises from the already operating wind turbines farms and pre-commercial tidal turbines arrays. Those configurations raise questions about turbine wakes interaction and loads fluctuations perceived by the downstream turbines. A critical need is therefore felt for a designing tool that represents properly such wakes interaction in a turbulent upstream flow. Recent studies analysed upstream turbulence influence on single turbine computations [1]. Other studies focused on wakes interaction in a steady inflow from an experimental [2] or numerical viewpoint [3]. While the insights on these separated phenomena are crucial, studies like [4] combining both upstream turbulence and wakes interaction are also needed. To meet this need, developments have been made on an in-house vortex particle (VP) solver named Dorothy [5, 6]. Upstream turbulence is taken into account using an adapted implementation of the synthetic eddy method (SEM) [7, 8]. Following ideas developed in the Lagrangian vortex community [9, 10], a new framework focusing on particles shedding has been developed to adapt a lifting-line (LL) blade representation into this VP solver, becoming Dorothy LL-VP [11].

The present study consists in the numerical reproduction of an experimental campaign led at IFREMER's wave and current flume tank on three scaled tidal turbine models [12, 13]. The objective is to assess whether Dorothy LL-VP is suited to reproduce turbine wakes interaction in terms of performance and flow behaviour. Following the experiments [12], two upstream conditions of different turbulence intensities (TI) are studied: a *low TI* ($\simeq 2$ %) and a *high TI* ($\simeq 15$ %). One of the turbines is located downstream of the two others. The downstream turbine can be placed at three different locations in order to study different levels of wakes interaction. For both upstream TI, the three spatial configurations are analysed to highlight the influence of wakes interaction and turbulence in the fluctuating loads perceived by the downstream turbine. In section 2, the underlying theoretical aspects behind Dorothy LL-VP solver are explained. The numerical set-up and turbine model input data are specified in section 3. The obtained results on wakes as well as on turbine loads are analysed and discussed in section 4.

2. Methodology: lifting-line embedded in a vortex particle solver

The local fluid vorticity is $\vec{\omega}$. In VP method, the fluid is discretised in $N \in \mathbb{N}$ particles. Particles properties are specifically denoted in uppercase letters. The i-th fluid particle position ($\vec{X}_i$), volume (V_i), vorticity weight ($\vec{\Omega}_i = \iiint_{V_i} \vec{\omega} dv$) and velocity ($\vec{U}_i$) time ($t$) variations are given by the discretised Lagrangian velocity-vorticity Navier-Stokes equations [14, 15]:

$$\frac{d\vec{X}_i}{dt}(t) = \vec{U}_i(t) = \underbrace{\vec{U}_i^\phi(t) + \vec{U}_i^\psi(t)}_{=[\vec{u}^H(\vec{x},t)]_{\vec{x}=\vec{X}_i(t)}} + \vec{U}_i'(t), \tag{1}$$

$$\frac{d\vec{\Omega}_i}{dt}(t) = \underbrace{\left[\left(\vec{\Omega}_i(t) \cdot \vec{\nabla}\right) \vec{u}^H(\vec{x},t)\right]_{\vec{x}=\vec{X}_i(t)}}_{=\vec{S}_i(t)}$$

$$+ \underbrace{V_i \left[\vec{\nabla}\nu_T(\vec{x},t) \times \Delta\vec{u}^H(\vec{x},t)\right]_{\vec{x}=\vec{X}_i(t)} + V_i \left[(\nu + \nu_T(\vec{x},t))\Delta\vec{\omega}(\vec{x},t)\right]_{\vec{x}=\vec{X}_i(t)}}_{=\vec{L}_i(t)}, \tag{2}$$

$$\frac{dV_i}{dt}(t) = 0. \tag{3}$$

Lowercase-denoted velocities are distinguished on purpose from the uppercase velocities that are reserved for particles description. Part of the velocity (Eq. (1)) comes from the Helmholtz velocity decomposition ($\vec{u}^H(\vec{X}_i(t), t)$). The potential velocity component ($\vec{U}_i^\phi$) comes from a scalar potential field (ϕ) and includes the mean upstream flow velocity ($\vec{u}^\infty$). The rotational velocity component ($\vec{U}_i^\psi$) comes from a divergence-free vector potential field ($\vec{\psi}$). It is evaluated using the Biot-Savart law (Eq. (4)) with the Moore-Rosenhead regularized kernel ($\vec{K}_\varepsilon$) of smoothing parameter ε [6, 14]. A *treecode* algorithm is used to lower the computational cost of the Biot-Savart law [6, 16].

$$\vec{U}_i^\psi(t) \simeq \sum_{j=1}^{N} \vec{K}_\varepsilon \left(\vec{X}_i(t) - \vec{X}_j(t)\right) \times \vec{\Omega}_j(t) \tag{4}$$

A velocity component ($\vec{U}_i'(t) = \vec{u}'(\vec{X}_i(t), t)$) representing upstream flow turbulence is added in Eq. (1). If there is no upstream turbulence, this component reduces to zero, otherwise it is evaluated using an adapted implementation of the synthetic eddy method (SEM) [7, 8]. The turbulent flow to be reproduced is known through its Reynolds stress tensor ($\overline{\overline{R}}$) and eddies integral length scale (L_I) [7]. The turbulent flow is reproduced in a volume (V_E) surrounding

the domain of study with $N_E \in \mathbb{N}$ eddies. Let x, y and z directions be represented by a respective integer in $[\![1,3]\!]$. The Cholesky decomposition of the Reynolds stress tensor gives a matrix $\overline{\overline{A}} = (a_{i,j})_{i,j \in [\![1,3]\!]}$ such that $\overline{\overline{R}} = \overline{\overline{A}}\,\overline{\overline{A}}^T$. The $m \in [\![1,3]\!]$ turbulent velocity component is:

$$u'_m(\vec{x}, t) = \sqrt{\frac{V_E}{N_E}} \sum_{k=1}^{N_E} F_{\lambda_k}\Big(\vec{x} - \vec{x}^k(t)\Big) \sum_{n=1}^{3} a_{m,n} \epsilon_{m,n}^k, \qquad (5)$$

with the k-th eddy properties: a random plus (source) or minus (sink) sign (ϵ^k), its position ($\vec{x}^k(t)$), and its shape function (F_{λ_k}) of base $2\lambda_k$ with the characteristic length (λ_k) evaluated using a random distribution of mean L_I. The momentum equation (Eq. (2)) stretching term ($\vec{S}_i(t)$) is written in its transposed formulation to ensure the total vorticity conservation [17]. It is directly evaluated by injecting the Biot-Savart law. The momentum equation (Eq. (2)) diffusion term ($\vec{L}_i(t)$) includes turbulent diffusion that accounts for large eddy simulation (LES) modelling [6]. Smagorinsky turbulent viscosity ($\nu_T(\vec{x}, t)$) model is used [18]. The diffusion term is computed via the particle strength exchange (PSE) method [19, 20]. The PSE provides a framework to estimate the Laplacian and gradient operators with dedicated Gaussian kernels of chosen accuracy [6]. Following a recently introduced idea [9, 10], a lifting-line blade representation [21] has been adapted from its initial filamentary approach to the present vortex particle background [11]. In this approach, the blade of length (L_b) is discretised in $N_s \in \mathbb{N}$ sections of width ($\mathrm{d}r = L_b/N_s$). Figure 1 represents a blade discretised in five sections with both the filamentary viewpoint and the specific VP adaptation. The blade leading edge (LE), trailing edge (TE) and angular velocity (ω_{rot}) are shown. The filamentary viewpoint is illustrated using the k-th contours-oriented panel at time (t) associated to a local bound circulation (Γ_B):

$$\Gamma_B = \frac{1}{2} c \|\vec{u}_t\| C_L. \qquad (6)$$

The local blade profile chord is c. The local true, or relative, velocity ($\vec{u}_t$) evaluation provides the local angle of attack (α) which allows to interpolate the lift coefficient (C_L) within tabulated data. The true velocity takes into account mean upstream velocity ($\vec{u}^\infty$), upstream turbulence influence ($\vec{u}'$), blade motion velocity, particles induced velocity (Eq. (4)) split into the wake particles and the particles shed at the current time (t). Three types of particles are identified:

- the k-th bound particle, associated to the k-th blade section, represents the solid lifting body. Its vorticity weight is defined by: $\vec{\Omega}_B = \Gamma_B(k,t)\mathrm{d}r\,\vec{e}_r(t)$;

- the trailing shed particles at the inter blade sections locations are represented. The trailing filaments lengths ($\|\vec{u}_t\|\mathrm{d}t$) vary along the blade. For long enough filaments, as shown at the $k+1$-th inter blade sections location, the vorticity is split into $N_T \in \mathbb{N}$ trailing shed particles. The vorticity weight ($\vec{\Omega}_{T,j}$) associated to the j-th trailing shed particle of the $k+1$-th inter blade section location is defined by the sum of contributions from the two adjacent panels: $\vec{\Omega}_{T,j} = \vec{u}_t(k+1)\mathrm{d}t(\Gamma_B(k,t) - \Gamma_B(k+1,t))/N_T$;

- the k-th spanwise shed particle vorticity weight ($\vec{\Omega}_S$) is defined by the sum of two contributions, one from the tail of the $\Gamma_B(k,t)$ panel and one from the head of the $\Gamma_B(k,t-\mathrm{d}t)$ panel: $\vec{\Omega}_S = \Gamma_B(k,t)(\vec{u}_t(k)\mathrm{d}t - \mathrm{d}r\vec{e}_r(t) - \vec{u}_t(k+1)\mathrm{d}t) + \Gamma_B(k,t-\mathrm{d}t)\mathrm{d}r\vec{e}_r(t-\mathrm{d}t)$.

A more in-depth description of the particles, including their shedding position, is available in [11]. Once trailing and spanwise shed particles are properly evaluated, they are added to the wake particles. Loads on the blade are evaluated using the tabulated lift and drag coefficients. A tip correction [22] is applied on the loads to circumvent the limited influence of tip vortex on the true velocity due to particles velocity smoothing [10, 11]. Integrating the loads provides turbine torque (Q) and thrust (T). Eventually, Navier-Stokes equations (Eq. (1) to Eq. (3))
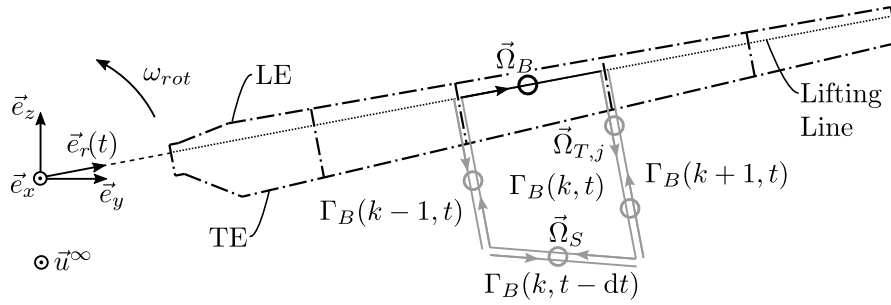
Figure 1: Lifting-line-represented rotating blade facing an upstream flow ($\vec{u}^\infty$). Bound particles (black circles) together with trailing and spanwise shed particles (grey circles) are represented.

are integrated with a second-order Runge-Kutta algorithm. Redistribution of the particles in the wake is performed at a user-prescribed multiple of the initial time-step. This redistribution algorithm replaces the old particles with new ones containing all the vorticity and located on a 3D cartesian grid. This is done to prevent from a too wide distortion of the particles distribution.

3. Numerical set-up and input data

The present study numerically reproduces an experimental campaign led at IFREMER's wave and current flume tank [12, 13]. Figure 2 represents the spatial configuration of the turbine models. One of the turbines is located four turbine diameters ($4D$) downstream of the two others. The downstream turbine is placed at three different positions on the $\vec{e}_y$ axis depending on the distance (d) between its rotation centre and the centreline of the light grey upstream turbine. As a matter of consistency with [12, 13], the downstream turbine position at $d = 1.0D$ is referred to as *config. 1*, $d = 0.75D$ as *config. 2* and $d = 0.5D$ as *config. 3*. Turbines of which performance are studied hereunder are represented in dark grey.
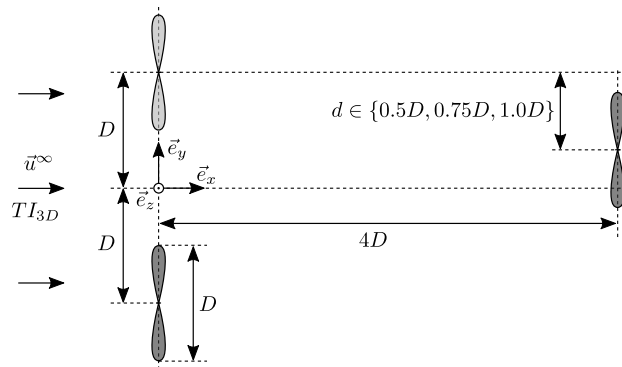

Figure 2: Spatial configuration of the three turbine models.

The turbine blade geometry corresponds to the IFREMER-LOMC model [6]. Compared to this former description, a global pitch is applied such that the tip blade section is at a zero pitch plus twist angle, see angles definition in [11]. This pitch matches the one of the experiments. NACA 63-418 and NACA 63-422 polar curves are computed using XFoil software [23] for small angles of attack and expanded with Viterna's method [24]. Experimental chord-based Reynolds number (Re) are evaluated around 10^5. Those values are in the transition region of the considered profiles. Hence, minor variations of Reynolds induce major changes in the associated polars. Furthermore, some uncertainties remain on the blades surface aspect and whether those profiles

represent the exact blade geometry. Therefore, in such uncertain conditions, XFoil fails to provide accurate polar curves. This is the reason why the Reynolds used to compute the polars is set at $Re \simeq 3.5 \times 10^5$ so as to minimise numerical torque and thrust error on a single LOMC-IFREMER turbine with respect to experimental results from [13]. Note that the presented LL-VP method has been previously validated with favourable comparison on performance, radial loads and wakes against cases with high quality polar curves: Mexnext-III study [11] and Oxford tidal benchmarking project [25]. Table 1 presents the turbine model properties : hub radius (R_h), blade length (L_b) ; as well as the chosen space and time discretisation : number of blade sections (N_s) and associated section width ($\mathrm{d}r = L_b/N_s$). The numerical angular velocity (ω_{rot}) matches the time-averaged experimental one. At this angular velocity, turbine models operate in their optimum performance area. Following [10, 11], the time-step ($\mathrm{d}t$) is chosen such that the angular step ($\mathrm{d}\theta$) is 5.0° per time-step.

Table 1: Turbine models properties and computational discretisation.

Pitch angle [°]	R_h [m]	L_b [m]	N_s [-]	$\mathrm{d}r$ [m]	ω_{rot} [rad·s^{-1}]	$\mathrm{d}\theta$ [°]	$\mathrm{d}t$ [s]
+4.87	0.046	0.304	20	0.015	8.0	5.0	0.011

Numerical upstream flow conditions, matching the experimental ones, are reported in Table 2. Two upstream conditions (referred to as *low TI* and *high TI*) are studied depending on the 3D turbulence intensity magnitude (TI_{3D}). The experimental data recorded one diameter ahead of the two upstream turbines, near the flume tank centreline, gives: mean upstream flow velocity ($\vec{u}^\infty$) along $\vec{e}_x$, standard deviations for the three velocity components (σ_{u_x}, σ_{u_y}, σ_{u_z}) together with other Reynolds stress tensor components and turbulent integral length scale (L_I). The 3D turbulence intensity is defined by: $TI_{3D} = (\sigma_{u_x}^2 + \sigma_{u_y}^2 + \sigma_{u_z}^2)^{1/2} / \left(3 \left(\overline{u_x}^2 + \overline{u_y}^2 + \overline{u_z}^2 \right) \right)^{1/2}$, where, for a given quantity q, the time average is denoted $\overline{q}$. Density (ρ) and kinematic viscosity (ν) of the water are set as: $\rho \simeq 10^3$ kg·m^{-3} and $\nu \simeq 10^{-6}$ m^2·s^{-1}.

Table 2: Upstream flow conditions for the two TI cases.

Case [-]	u^∞ [m·s^{-1}]	σ_{u_x} [m·s^{-1}]	$\sigma_{u_y} = \sigma_{u_z}$ [m·s^{-1}]	L_I [m]	TI_{3D} [%]
Low TI	0.79	0.02	0.01	0.7	2.0
High TI	0.80	0.12	0.12	0.7	15.0

4. Results and discussion

All the computations have been run on 576 CPUs on AMD EPYC 9654 Genoa nodes with a wall-clock time of 24 hours. This choice is made to balance memory allocation issues and computational resources. This leads to a significant change in the maximum physical time reached by *low TI* (approx. 30 s) and *high TI* (approx. 20 s) computations. The wider domain generated by the high turbulence intensity, thus requiring more particles, easily explains this difference in the computational cost. The first ten seconds of each computation are needed to fully establish the wakes. Hence, all the results presented in this section are averaged on the last 20 s for the *low TI* cases and on the last 10 s for the *high TI* cases. Such time series appears to be shorter than what is needed for proper statistics convergence, mainly for *high TI* cases. This is the reason why performance averages and standard deviations of the downstream turbine are not presented in subsection 4.2.

4.1. Wakes analysis

Figure 3 presents the numerical 2D wake maps of averaged velocity component u_x. The different spatial configurations are represented, from 1 to 3 respectively, on Fig. 3a, Fig. 3c, Fig. 3e for the *low TI* cases and Fig. 3b, Fig. 3d, Fig. 3f for the *high TI* cases. The downstream turbine is most immersed in upstream turbine wakes in config. 3, when its rotation centre is the closest to one of the upstream turbines centreline. It is observed that the shortening of the turbines wakes length, from $10D$ to around $\simeq 5D$, with the increased upstream turbulence is numerically well captured in spite of the limited averaging time. However, it appears that this shortening does not prevent the downstream turbine from being impacted by upstream turbine wakes. Various wake shapes are noticed across the different *high TI* cases. This shows the need for longer computation time. Finally, the absence of hub in the turbines modelling is noticeable. It significantly affects the obtained mean wakes with this "nozzle" effect seen at the rotation centre of each turbine.

Figure 4 presents the same numerical data as figure 3 but with one-dimensional velocity profiles at given x-positions. Those numerical results are confronted to the experimental ones. Generally, a good agreement is obtained between numerical and experimental results for all the spatial configurations at both turbulent intensities. To the authors opinion, the observed discrepancies may partly come from the polar curves used in the numerical computations. Moreover, the absence of hub modelling in the numerical results is a major source of discrepancy for the profiles evaluated just downstream of the turbines ($x = 2D$ and $x = 5.2D$). Finally, the 9.6 % flume tank blockage, generated by the limited depth in between the flume tank floor and the
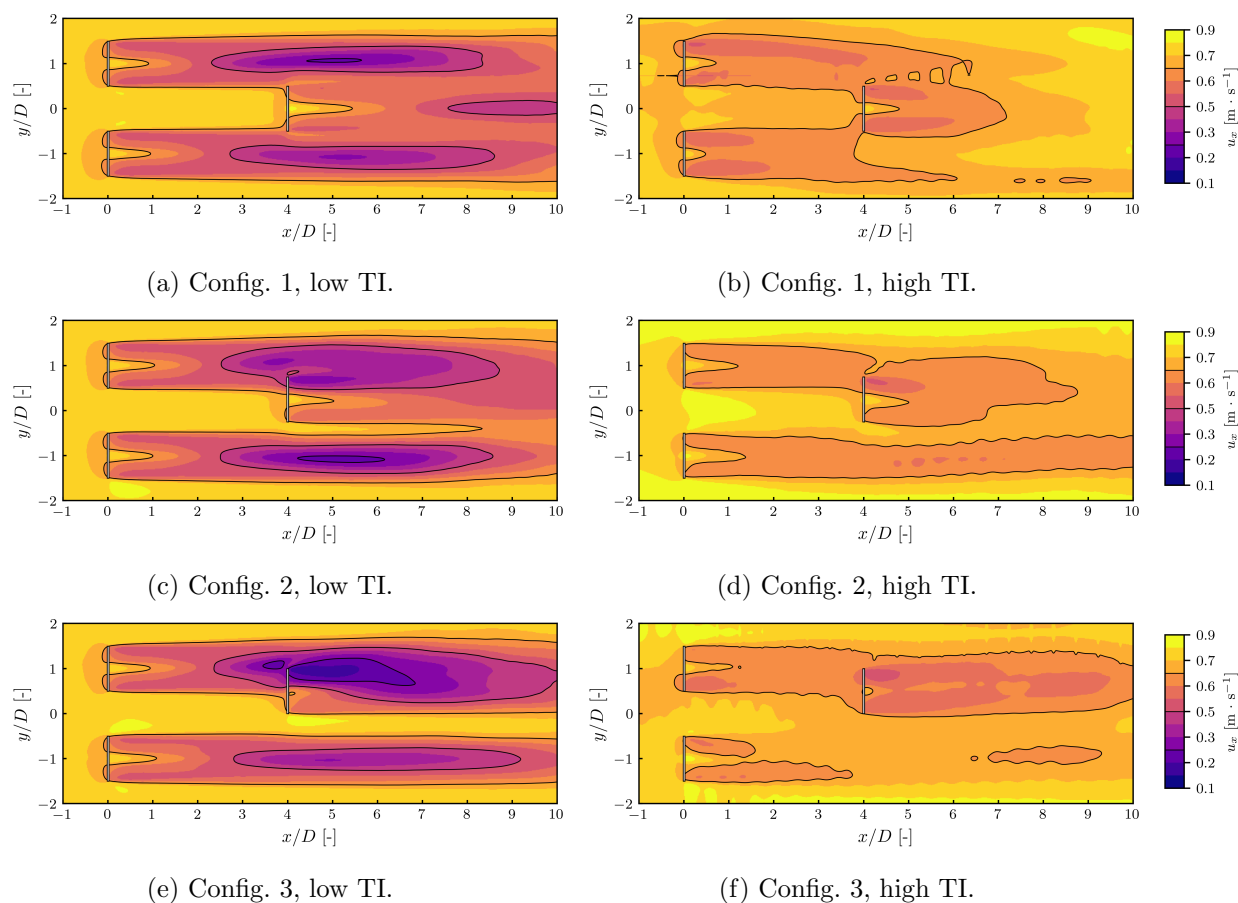

(a) Config. 1, low TI.

(b) Config. 1, high TI.

(c) Config. 2, low TI.

(d) Config. 2, high TI.

(e) Config. 3, low TI.

(f) Config. 3, high TI.

Figure 3: Numerical velocity (u_x) wake maps.

(a) Config. 1, low TI.

(b) Config. 1, high TI.

(c) Config. 2, low TI.

(d) Config. 2, high TI.
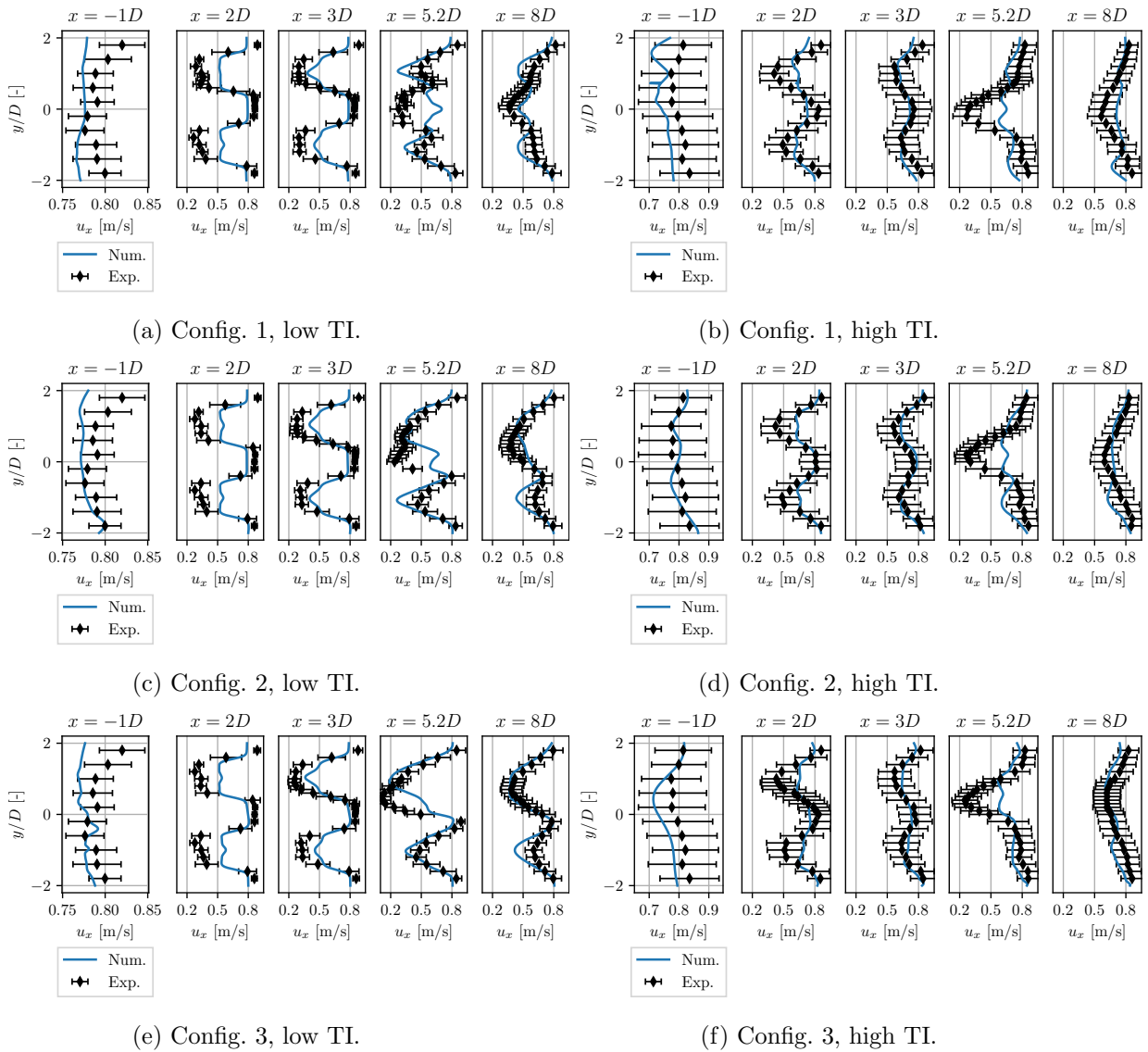
(e) Config. 3, low TI.

(f) Config. 3, high TI.

Figure 4: Velocity (u_x) profiles comparison between numerical and experimental results.

free-surface, leads to a slight over-speed in the inter-turbine spacings ($x = 2D$ and $x = 3D$). This experimental phenomenon slightly enhances the downstream turbine performance and energy extraction which in turn slightly increases the velocity depletion after this turbine ($x = 5.2D$).

4.2. Performance analysis

The present section focuses on numerical results to avoid misleading comparisons with experimental results due to aforementioned input data limitations and fixed angular velocity assumption. Turbines performance are assessed using power (C_P) and thrust (C_T) coefficients:

$$C_P = \frac{\omega_{rot} Q}{\frac{1}{2} \rho \pi \left(L_b + R_h\right)^2 \|\vec{u}^\infty\|^3}, \qquad C_T = \frac{T}{\frac{1}{2} \rho \pi \left(L_b + R_h\right)^2 \|\vec{u}^\infty\|^2}. \qquad (7)$$

The frequency content of the performance is studied by means of the power spectral density (PSD) [26]. For a given quantity q, its PSD is denoted S_{qq}. Torque (S_{QQ}) and thrust (S_{TT}) PSDs

are studied hereunder. Figure 5 presents performance results for the three spatial configurations in the *low TI* upstream conditions. Power (C_P) and thrust (C_T) coefficients as functions of time (t) are shown respectively in Fig. 5a and Fig. 5b. Torque (S_{QQ}) and thrust (S_{TT}) PSDs as a function of the frequency (f) are respectively reproduced in Fig. 5c and Fig. 5d. Similarly, figure 6 presents the same results for the *high TI* upstream conditions. The three solid lines present the downstream turbine results, each one for a different spatial configuration. The dashed line presents the dark grey (see Fig. 2) upstream turbine results as a reference.

Time domain power and thrust coefficients fluctuations are significant for all cases. The more the downstream turbine is immersed in the upstream one wake, the higher the fluctuations are and the lower the average performance is. The downstream turbine highest loads fluctuations are recorded in the *high TI* config. 3 case. Moreover, high loads fluctuations at $3f_{rot}$ and $6f_{rot}$ frequencies in the PSDs spectra are observed mainly for the downstream turbine in config. 2 and config. 3. The relative magnitude of those components is lower in *high TI* cases compared to *low TI* cases. This is understood as an influence of wake mixing and shortening induced by the higher upstream turbulence intensity in the *high TI* conditions. Furthermore, a $-11/3$ slope in the PSDs spectra is noticed. It is an expected turbine response when the upstream turbulence spectrum is characterised by a $-5/3$ slope in the inertial subrange. This has been

(a) C_P, low TI.

(b) C_T, low TI.

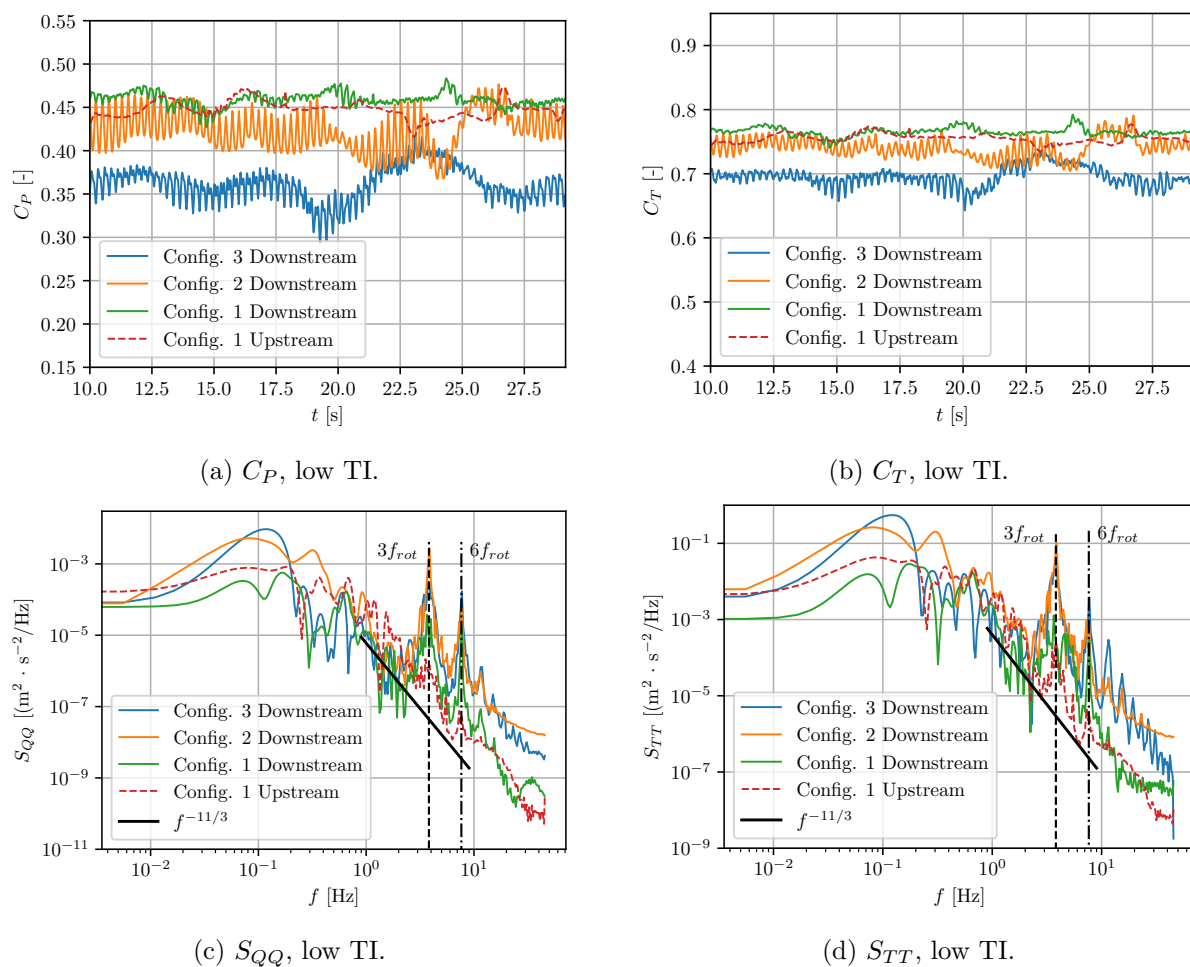(c) S_{QQ}, low TI.

(d) S_{TT}, low TI.

Figure 5: Performance study in time and frequency domains for the *low TI* upstream conditions. Solid lines refer to the downstream turbine and the dashed line to the upstream one.

(a) C_P, high TI.

(b) C_T, high TI.

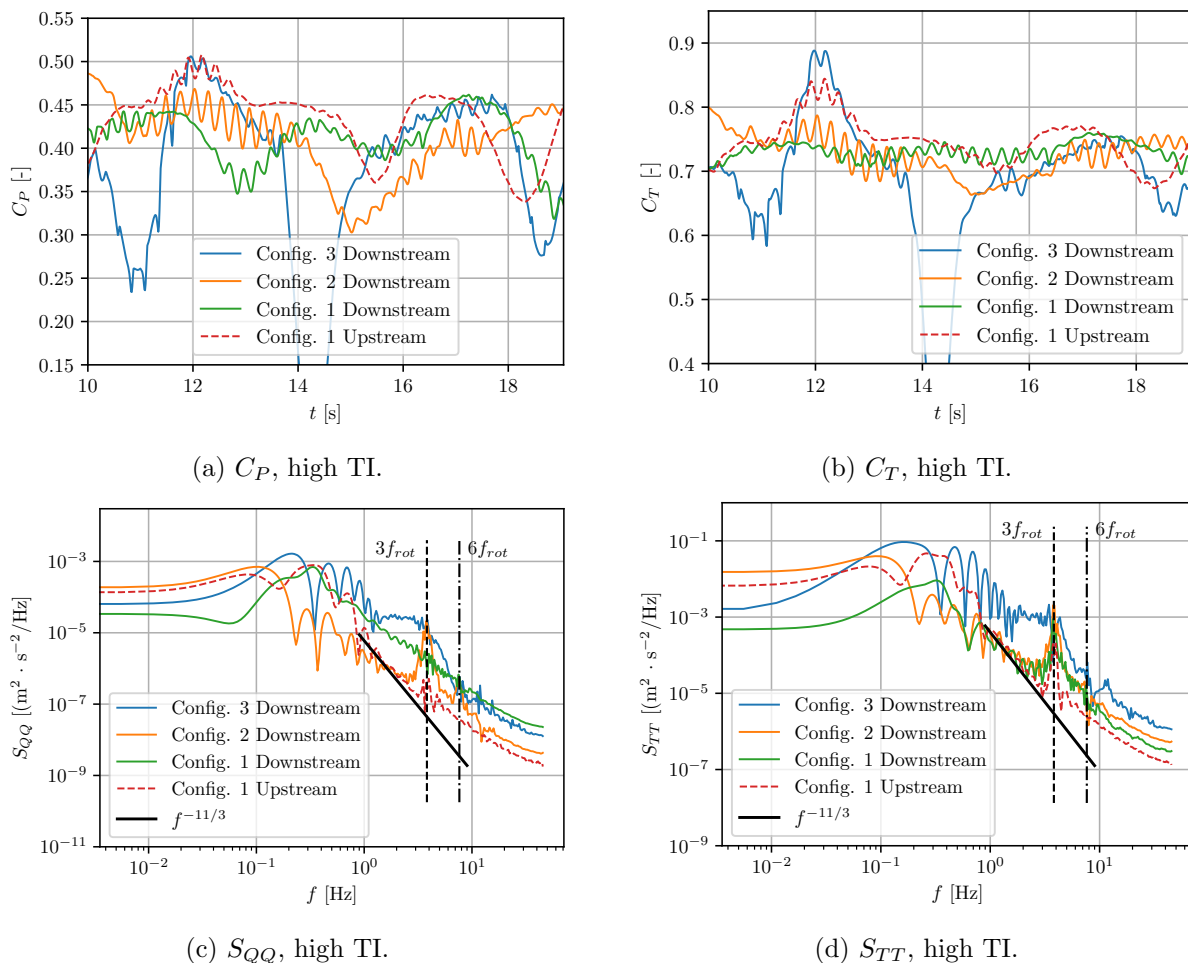

(c) S_{QQ}, high TI.

(d) S_{TT}, high TI.

Figure 6: Performance study in time and frequency domains for the *high TI* upstream conditions. Solid lines refer to the downstream turbine and the dashed line to the upstream one.

thoroughly analysed for both wind and tidal turbines in [27, 28]. Nevertheless, this behaviour is less discernible for the *high TI* cases.

Eventually, the current turbine modelling in Dorothy LL-VP is based on a fixed angular velocity (ω_{rot}). However, real-life devices, including the turbine models used in the experiment, need a controller to keep their angular velocity as close as possible to the desired input value. This leads to time-dependent angular velocity variations reaching ± 2 % of the average in the experiment. Such angular velocity variations must generate loads fluctuations which are thus not captured in the present numerical study. Hence, adding an angular velocity controller in the numerical modelling must enhance downstream turbine loads fluctuations prediction.

5. Conclusion

The current study presents numerical results on three tidal turbine models in a turbulent upstream flow with wakes interaction using a lifting-line coupled to a vortex particle solver: Dorothy LL-VP. A good agreement is obtained between numerical and experimental results on wakes and velocity profiles. Preliminary performance results on the downstream turbine predict high fluctuations together with an experimental-like behaviour in the frequency domain. The methodology and its capabilities can be transposed to the wind energy field. Interesting

perspectives follow this study: results on longer computations, adding a hub representation and a controller in the turbine numerical modelling in order to improve farm simulations.

Acknowledgment

References
[1] Mullings H and Stallard T 2022 *Journal of Fluids and Structures* **114** 103698 ISSN 08899746

[2] Krogstad P Å and Sætran L 2015 *Journal of Physics: Conference Series* **625** 012043 ISSN 1742-6588, 1742-6596

[3] Onel H C and Tuncer I H 2020 *Journal of Physics: Conference Series* **1618** 062009 ISSN 1742-6588, 1742-6596

[4] Yang X, Boomsma A, Barone M and Sotiropoulos F 2014 *Journal of Physics: Conference Series* **524** 012139 ISSN 1742-6596

[5] Pinon G, Mycek P, Germain G and Rivoalen E 2012 *Renewable Energy* **46** 111–126 ISSN 0960-1481

[6] Mycek P 2013 *Étude Numérique et Expérimentale Du Comportement d'hydroliennes* Ph.D. thesis Université du Havre

[7] Jarrin N, Benhamadouche S, Laurence D and Prosser R 2006 *International Journal of Heat and Fluid Flow* **27** 585–593

[8] Choma Bex C, Carlier C, Fur A, Pinon G, Germain G and Rivoalen É 2020 *Applied Mathematical Modelling* **88** 38–54 ISSN 0307-904X

[9] Chatelain P, Backaert S, Winckelmans G and Kern S 2013 *Flow, Turbulence and Combustion* **91** 587–605 ISSN 1386-6184, 1573-1987

[10] Ramos-García N, Hejlesen M M, Sørensen J N and Walther J H 2017 *Wind Energy* **20** 1871–1889 ISSN 1095-4244, 1099-1824

[11] Dufour M A, Pinon G, Rivoalen E, Blondel F and Germain G 2024 *Wind Energy* **27** ISSN 1095-4244, 1099-1824

[12] Gaurier B, Germain G, Facq J V, Bacchetti T, Carlier C and Pinon G 2018 Three tidal turbines in interaction: An experimental data-set on wake and performances.

[13] Gaurier B, Carlier C, Germain G, Pinon G and Rivoalen E 2020 *Renewable Energy* **148** 1150–1164 ISSN 0960-1481

[14] Winckelmans G S and Leonard A 1993 *Journal of Computational Physics* **109** 247–273 ISSN 0021-9991

[15] Cottet G H and Koumoutsakos P D 2000 *Vortex Methods: Theory and Practice* (Cambridge ; New York: Cambridge University Press) ISBN 978-0-521-62186-1

[16] Lindsay K and Krasny R 2001 *Journal of Computational Physics* **172** 879–907 ISSN 0021-9991

[17] Choquin J P and Cottet G H 1988 *Comptes Rendus Hebdomadaires des Séances de l'Académie des Sciences* **306** 739–742

[18] Smagorinsky J 1963 *Monthly Weather Review* **91** 99–164

[19] Degond P and Mas-Gallic S 1989 *Mathematics of Computation* **53** 509–526

[20] Choquin J and Huberson S 1989 *Computers & Fluids* **17** 397–410 ISSN 0045-7930

[21] van Garrel A 2003 *Energy research Centre of the Netherlands*

[22] Shen W Z, Mikkelsen R, Sørensen J N and Bak C 2005 *Wind Energy* **8** 457–475 ISSN 1095-4244, 1099-1824

[23] Drela M and Giles M B 1987 *AIAA Journal* **25** 1347–1355 ISSN 0001-1452, 1533-385X

[24] Viterna L A and Janetzke D C 1982 Theoretical and experimental power from large horizontal-axis wind turbines Tech. Rep. DOE/NASA/20320-41; NASA-TM-82944 NASA Lewis Research Center

[25] Willden R, Chen X, Tucker Harvey S, Edwards H, Vogel C, Bhavsar K, Allsop T, Gilbert J, Mullings H, Ghobrial M, Ouro P, Apsley D, Stallard T, Benson I, Young A, Schmitt P, Zilic De Arcos F, Dufour M A, Choma Bex C, Pinon G, Evans A, Togneri M, Masters I, Da Silva Ignacio L, Duarte C, Souza F, Gambuzza S, Liu Y, Viola I, Rentschler M, Gomes T, Vaz G, Azcueta R, Ward H, Salvatore F, Sarichloo Z, Calcagni D, Tran T, Ross H, Oliveira M, Puraca R and Carmo B 2023 *Proceedings of the European Wave and Tidal Energy Conference* **15** ISSN 2706-6940, 2706-6932

[26] Welch P 1967 *IEEE Transactions on Audio and Electroacoustics* **15** 70–73 ISSN 0018-9278

[27] Tobin N, Zhu H and Chamorro L P 2015 *Journal of Turbulence* **16** 832–846 ISSN 1468-5248

[28] Druault P, Gaurier B and Germain G 2022 *Renewable Energy* **181** 1062–1080 ISSN 09601481